

Titre: Mechanical characterization of an origami-inspired super
Title: deformable metamaterial with high tunability for tissue engineering

Auteurs: Mohammad Ali Bagheri, Carl-Éric Aubin, Marie-Lyne Nault, & Isabelle
Authors: Villemure

Date: 2025

Type: Article de revue / Article

Référence: Bagheri, M. A., Aubin, C.-É., Nault, M.-L., & Villemure, I. (2025). Mechanical
Citation: characterization of an origami-inspired super deformable metamaterial with high
tunability for tissue engineering. *Materials & Design*, 251, 113701 (13 pages).
<https://doi.org/10.1016/j.matdes.2025.113701>

Document en libre accès dans PolyPublie

Open Access document in PolyPublie

URL de PolyPublie:
PolyPublie URL: <https://publications.polymtl.ca/62639/>

Version: Version officielle de l'éditeur / Published version
Révisé par les pairs / Refereed

Conditions d'utilisation: Creative Commons Attribution-Utilisation non commerciale-Pas
Terms of Use: d'oeuvre dérivée 4.0 International / Creative Commons Attribution-
NonCommercial-NoDerivatives 4.0 International (CC BY-NC-ND)

Document publié chez l'éditeur officiel

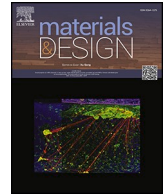
Document issued by the official publisher

Titre de la revue: Materials & Design (vol. 251)
Journal Title:

Maison d'édition: Elsevier
Publisher:

URL officiel: <https://doi.org/10.1016/j.matdes.2025.113701>
Official URL:

Mention légale:
Legal notice:



Mechanical characterization of an origami-inspired super deformable metamaterial with high tunability for tissue engineering[☆]

M.A. Bagheri^{a,b}, C.E. Aubin^{a,b,c}, M.L. Nault^{b,c}, I. Villemure^{a,b,*}

^a Polytechnique Montréal, Biomedical Engineering Institute, 2500 Ch. de Polytechnique, Montréal, QC H3T 1J4, Canada

^b CHU Sainte-Justine, 3185 Chemin de la Côte Ste-Catherine, Montréal, QC H3T 1C5, Canada

^c Université de Montréal, 2900 boul. Edouard-Montpetit, Montréal, QC H3T 1J4, Canada

ARTICLE INFO

Keywords:

Metamaterial
Tissue engineering
Finite element method
Origami
Gaussian process regression
Additive manufacturing

ABSTRACT

Origami-inspired metamaterials have gained significant attention for their ability to mimic the complex mechanical behavior of biological tissues and their potential applications in advanced surgical treatments. Inspired by Kresling origami, we introduced a metamaterial capable of large recoverable deformations. A parametric design explored the effects of changing geometrical parameters on the mechanical properties of the metamaterial. Eighteen designs were fabricated and mechanically tested for practicability assessment and validation purposes. Non-linear finite element method was leveraged to test the entire design space of the metamaterial. Using Bayesian machine learning, the sensitivity of surface to volume ratio, porosity, elastic modulus, strain energy density, and maximum local strain to the design inputs was assessed and their corresponding predictive models were created. The fabricated designs could withstand 80 % and up to 70 % recoverable strain in quasi static and cyclic loading, respectively, while exhibiting a wide range of structural and mechanical properties. From predictive models, elastic modulus of 0.1 Pa to 1.8 KPa was attainable, while having porosities from 49.7 % to 99.9 %. This study demonstrated the feasibility of the design and manufacturing of an origami-inspired super deformable metamaterial with highly-tunable structural and mechanical properties, which can be used for various tissue engineering applications.

1. Introduction

There has been a growing interest in the application of 3D printed scaffolds for tissue engineering [1–4]. For instance, large bone defects, which have a high likelihood of non-union and failure have been successfully treated in large animal models by using tissue engineered scaffolds [5,6], which shows the great potential of translating these complementary treatments into clinic [7]. However, finding scaffold architectures that can achieve suitable mechanical and structural properties remains a design challenge. Several 3D architecture patterns, such as grid [6], honeycomb [8], and triply periodic minimal surface [9], have been investigated. These structures can attain a range of stiffness and porosity by modifying design parameters such as wall thickness, and material composition [8,10–12]. However, in order to achieve extreme mechanical properties, such as super compressibility or negative Poisson's ratio, new design concepts should be implemented.

Metamaterials inspired from origami patterns can exhibit flat foldability with tunable mechanical properties [13–15]. By changing the

magnitude of geometrical inputs, such as angles, and crease length, different mechanical properties can be achieved [13,15,16]. Kresling pattern is an origami pattern that can be created by segmenting a sheet of paper into a row of triangles connected to each other, folding the segmentation lines to create mountains and valleys in the planar state, and connecting the first and the last triangle to make the 3D state [16–18]. The concept of removing panels from the Kresling pattern and replacing it with flexible linkage to create metamaterials with tunable stiffness has been introduced in previous studies [17,19]. However, these metamaterials were manually assembled from several non-biocompatible components in a scale larger than biological tissues [17,19]. Moreover, the sample size for experimentations was small, which weakened the predictability of the mechanical behavior of the metamaterials [15,16]. This suggests that designing scaffolds inspired by origami patterns is likely the approach to obtain super deformability in tissue engineering scaffolds, but the final outcome is highly dependent on the manufacturing process.

Optimizing a design for scaffolds to get the best outcome for tissue

[☆] This article is part of a special issue entitled: 'AI Materials' published in Materials & Design.

* Corresponding author.

regeneration remains a challenge due to its multi-parametric nature [20,21]. The regenerative capacity of scaffolds depends on several factors such as material composition, surface topology, and structural property [3,10,22]. For instance, for load-bearing scaffolds for bone healing, characteristics such as elasticity, porosity, and free surface to volume ratio have shown to impact bone regeneration outcomes [22]. Studies reported that using scaffolds with materials with lower Young's modulus enhances bone healing [22]. Highly porous scaffolds with interconnected structure promote angiogenesis and cell growth [8,23], and the effect of free surface to volume ratio on bone growth is still a place of debate [22,24,25]. Hence, identifying the key structural parameters influencing the performance of scaffolds and creating predictive models are essential for tuning the design for different applications.

Fabrication of highly porous and geometrically complex metamaterials demands additive manufacturing modalities that allow free-form printing. Selective laser sintering (SLS) is suitable as unsintered powder will support the printed structure. Feasibility of fabricating highly porous scaffolds by SLS printing with resulting high strain tolerance has been established in former studies [11,26,27]. This widely extends the design possibilities, and enables the creation of sophisticated metamaterials in large scale.

The objective of the present study was to introduce a design concept of an origami inspired super compressible metamaterial (OISCM), to fabricate and conduct a comprehensive structural and mechanical characterization of OISCM. We hypothesize that OISCM can have wide range of mechanical properties while preserving its recoverable super compressibility.

2. Materials and methods

2.1. Design of an origami inspired metamaterial

The design of OISCM consists of two struts forming a triangular shape tessellating through the lateral surface of a cylindrical cell with height h , and diameter d_{cell} (Fig. 1a). Out of the horizontal plane, two struts each with identical circular cross sections with a diameter d_{strut} connect the bottom and top disk of the cell (Fig. 1a). By having the number of triangles (n), the location of struts can be set by evenly distributing them around the bottom circular edge of the cell. The end of the struts coincides at the top circular edge of the cell at a point which has a rotation angle of ϕ relative to the bottom (Fig. 1a). In order to develop the parametric design of OISCM, h was assumed to remain constant and equal to 10 mm, while $0.1 \text{ mm} < d_{strut} < 0.7 \text{ mm}$, $0^\circ < \phi < 60^\circ$, $6 < n < 36$, and $10 \text{ mm} < d_{cell} < 50 \text{ mm}$ were defined as possible input variables.

2.2. Fabrication and super compressibility assessment of OISCM by experiment

Nine design groups of the OISCM were selected for fabrication and

mechanical experiment (Fig. 1b) with the details provided in Table 1. Each design group consisted of the same inputs except for d_{cell} , which was 20 mm and 40 mm. Computer-aided design (CAD) of each sample was automatically generated using a customized Python script in ABAQUS V6.24 (Vélizy-Villacoublay, France). A volume of interest (VOI) was defined as the smallest cylinder that can fit the struts inside. The minimum outer radius of the cylinder (r_{out}) was calculated by:

$$r_{out} = \left(\frac{d_{cell}}{2} + \frac{d_{strut}}{2} \right)$$

To calculate the maximum inner radius of the cylinder (r_{in}), point 1 and 2 were defined as points at the intersection of the longer strut (red strut in Fig. 1a) and bottom disc and top disc, respectively. The coordinates of the points were:

$$\text{Point 1 coordinates} = \begin{pmatrix} x_1 = \frac{d_{cell}}{2} \\ y_1 = 0 \\ z_1 = 0 \end{pmatrix}$$

$$\text{Point 3 coordinate} = \begin{pmatrix} x_2 = \frac{d_{cell}}{2} \cos\left(\frac{2\pi}{n} + \phi\right) \\ y_2 = \frac{d_{cell}}{2} \sin\left(\frac{2\pi}{n} + \phi\right) \\ z_2 = h \end{pmatrix}$$

r_{in} and VOI were then calculated as:

$$r_{in} = \left(\sqrt{\left(\frac{x_1 + x_2}{2}\right)^2 + \left(\frac{y_1 + y_2}{2}\right)^2} \right) - \frac{d_{strut}}{2}$$

$$VOI = \pi(r_{out}^2 - r_{in}^2)h$$

The porosity (P) and surface area to volume ratio (S/V) of OISCM corresponding to each design point were calculated by the following equations:

$$P = \frac{VOI - V_{solid}}{VOI} \times 100$$

$$S/V = \frac{S}{V_{Total}}$$

where V_{solid} and S were volume of the solid parts and surface area of the solid parts in the VOI, respectively, extracted directly from the models. STL files of the designs were generated and exported from ABAQUS to Sinterit Studio (Version 3.6, EOS GmbH) for slicing to layers of 50 μm , with a laser scanning speed of 1500 mm/s. Six samples for each selected design were fabricated by SLS 3D printing using Lisa Pro (Sinterit Sp. z o. o., Kraków, Poland). The printed material was Flexa gray, a commercially available powder from Sinterit (Poland, Kraków) for SLS 3D

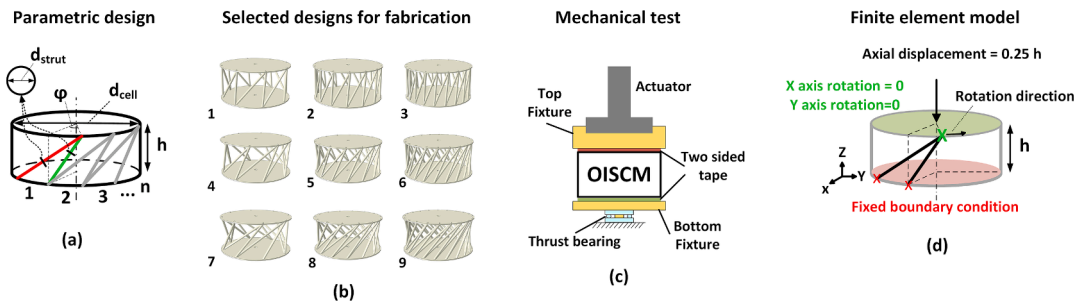
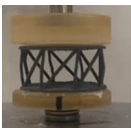
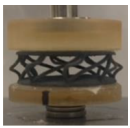
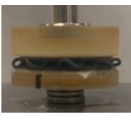

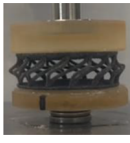

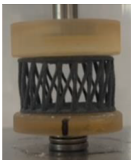
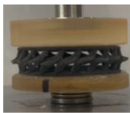

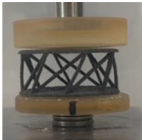
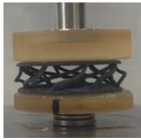
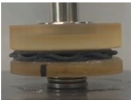
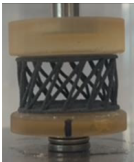
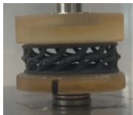





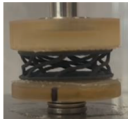
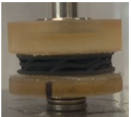
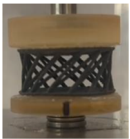
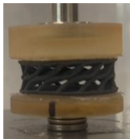
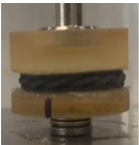

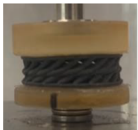
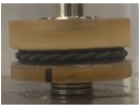


Fig. 1. (a) Parametric design of the OISCM with d_{strut} , ϕ , n , and d_{cell} as input variables, and h as input constants. (b) Computer aided designs corresponding to 9 different combinations of input variables selected for fabrication and mechanical testing. (c) Mechanical testing setup to apply axial displacement to OISCM samples. (d) Reduced FE model with struts connected from the bottom disc to the top disc. Bottom end of the struts had no degrees of freedom. Top end of the struts could have rotation only about the z axis. The translational movement was free in all directions.

Table 1
Input variable set for each selected design, the corresponding printed samples, and visualization of the response to a quasi-static strain up to 80 %.

Group	Input parameters				Mechanical Experiment		
	d _{strut} (mm)	Φ (°)	n	d _{cell} (mm)	Fabrication	Apparent strain (%)	
					0	50	80
1	0.55	5	8	20, 40			
2	0.55	5	14	20, 40			
3	0.55	5	20	20, 40			
4	0.55	25	8	20, 40			
5	0.55	25	14	20, 40			
6	0.55	25	20	20, 40			
7	0.55	45	8	20, 40			
8	0.55	45	14	20, 40			
9	0.55	45	20	20, 40			

printing.

Each sample was fixed in all degrees of freedom at the top disc by using a double sided tape, while was free to have rotation about its cylindrical axis at the bottom disc by using a customized revolute joint with a thrust bearing (Fig. 1c). Samples were then subjected to a quasi-static uniaxial compression apparent strain of 80 % (Table 1) at a crosshead speed of 2 mm/min to investigate the initial mechanical property, and to 10 %, 30 %, 50 %, 70 % uniaxial compression apparent strain for 200 cycles with a loading frequency of 1Hz to assess the recover capability of the metamaterial [11]. All the tests were done using a Mach-1 micromechanical system (Biomomentum Inc., Laval, QC, Canada). The Load-displacement data was recorded with a load cell of 100N. By dividing the reaction load to the cross section of OISCM and dividing the displacement of the actuator to h apparent stress and apparent strain were calculated, respectively. The stress-strain graphs of each sample was separated to three regions based on the general behavior of porous structures under compression [11,13]: Linear region for the calculation of the elastic modulus; Plateau region with zero or negative stiffness due to buckling; and densification region with increased stiffness due to contacts of struts. Apparent elastic modulus of each sample was calculated from the linear region as follows:

$$E = \frac{F_r/A}{\epsilon} = \frac{F_r/\pi r_{out}^2}{\Delta h/h_0}$$

where F_r is the reaction force, A is area of the discs, ϵ is the apparent strain of the metamaterial, Δh is the height change of the metamaterial, h_0 is the initial height, and r_{out} is the outer radius of the discs. Stress at which the plateau region initiated was recorded as critical buckle stress. Strain at which the densification region started was recorded as the densification limit. To quantify the non-linear behavior of the metamaterial, strain energy density (U) was calculated as follows:

$$U = \int_0^\epsilon \sigma d\epsilon$$

where the area under the stress-strain curve for $\epsilon = 25\%$ was calculated using the Simpson's rule [28].

2.3. Statistical analysis

Experimental data was described as mean \pm standard deviation. One-way ANOVA and Tukey multiple pairwise comparison was conducted. P value smaller than 0.05 was considered as statistically significant. Only relevant statistical relationships are presented in figures.

2.4. Development of a finite element model of OISCM

Non-linear finite element analysis was implemented to computationally predict the initial deformation of struts due to axial displacement at the top disc of the OISCM (Fig. 1b). The struts were meshed with ten-node tetrahedral elements to be able to mesh complex geometries at the merging region of the two struts. Mesh convergence analysis showed that at least 12 elements in the perimeter of the struts is required to achieve mesh independence of the outputs. Therefore, the mesh size was defined as follows:

$$Meshsize = \frac{\pi d_{strut}}{k}, k \geq 12$$

where k is the minimum number of elements in the perimeter of the struts required to achieve mesh independency. Flexa gray was assumed as an isotropic material with linear elastic modulus of 13.78 MPa and Poisson's ratio of 0.35, and elongation at break of 130 %, which was derived from bulk SLS 3D printed samples and was assigned to the struts. This mechanical properties corresponds to biomaterials such as high molecular weight PCL [11]. The top end of the struts attached to the top disc were free to rotate about the z axis and have translation in the x, y

and z directions, while having zero rotation about the x and y axis to avoid tilting of the top disc. The bottom end of the struts attached to the bottom disc were fixed in all degrees of freedom. A compressive load was applied at the top end of the OISCM (Fig. 1b).

To capture the non-linear buckling behaviour of struts, the arc-length method was implemented [29,30]. First, buckle analysis was done in ABAQUS to find three different buckling modes of the struts. The first buckling mode was chosen as it was similar to the buckling mode of the fabricated prototypes and most likely to happen. As a linear material was assumed to make the struts and no geometrical non-linearity was expected before the buckling, confirmed by the stress-strain graphs from the experiments, a linear eigenvalue analysis was implemented with Riks method, in which geometrical imperfections from the linear buckle analysis (first buckle mode) were used as an input to the Riks solver to capture the post buckling non-linearity of the struts.

2.5. Verification and validation

Uncertainty quantification was undertaken by assessing the effect of introducing different magnitudes of imperfections on the non-linear behavior of the system. Imperfection was applied to the nodes coordinates of each of the 9 models. The magnitude of the imperfections was controlled by defining an imperfection multiplier (IM): 2, 1.5, 1, 0.5, 0.25, 0.125, 0.062, and 0.032. It was found that applying less than 25 % of the geometrical imperfections (IM = 0.25) minimizes its effect on the stress-strain response of the system, while causing no convergence issue. For the simulation of the nine selected samples in the experiments, effect of all the IMs were simulated and reported as stress-strain graphs of each design with an average and confidence intervals. The FE model was then validated against the experiments. An IM of 0.5 was used for the simulation of the 1500 samples for calibrating the FEA with the experimental results.

2.6. Virtual lab and data-driven Bayesian machine learning

An automated virtual lab was created to investigate structural and mechanical properties of OISCM. Using a Sobol sequence, 1500 samples were defined within the design space (Fig. 2a). The 3D CAD model corresponding to each design point was generated and the corresponding P and S/V were calculated with the same approach as in the selected samples. The FE model corresponding to each design point was generated. In order to minimize the computational cost and avoid convergence issues, each sample was reduced to its two building struts (Fig. 1d) based on the assumption that the struts have no contact during the compression and the principle of superposition [29]. Therefore, the simulations were limited to the apparent strains less than 25 %, which was found to be the minimum apparent strain in which strut contact occurred in the experiments. This apparent strain corresponded to a OISCM design point with $d_{strut} = 0.6$ mm, $\phi = 60^\circ$, $n = 36$, $d_{cell} = 20$ mm, which was quite an extremity in the design space. The response of each design point was recorded as equivalent stress-strain graphs, and maximum local principal strain in the struts (ϵ_{max}). E and U were calculated with the same approach as in the mechanical tests (Fig. 2c).

An input vector consisted of (d_{strut} , ϕ , n , d_{cell}) for the 1500 samples was generated and associated with the corresponding output vector of (P, S/V, E, ϵ_{max} , U). A variance-based Sobol global sensitivity analysis was then conducted using SALib [31] library to assess the impact of each input variable on the outputs. Following the sensitivity analysis, a predictive model was developed for each output using Bayesian machine learning, specifically Gaussian Process Regression (GPR) using GPflow [32]. GPR is a non-parametric, probabilistic model that provides a measure of uncertainty along with predictions [21,29,33], making it particularly suitable for our study as we dealt with uncertainties related to the magnitude of geometrical imperfection. The GPR model utilized a Matern 5/2 kernel with Automatic Relevance Determination (ARD) to model the relationships in the design space. The optimization of the GPR

Virtual lab for data driven Bayesian machine learning

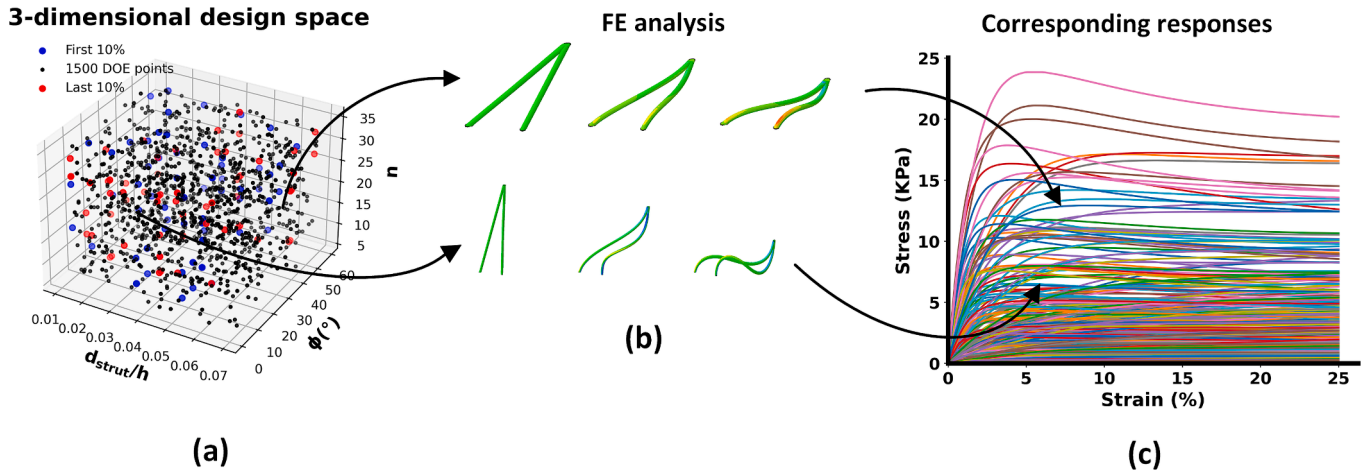


Fig. 2. (a) Design space of the OISCM generated by Sobol sequence. To show the uniform distribution of the samples in the design space first and last 10 % of the 1500 designing points were highlighted in blue and red, respectively. (b) Buckling behaviour and local strain contour of two different designs of the OISCM due to the defined displacement and boundary conditions. (c) Equivalent stress-strain graphs of the entire samples with linear and nonlinear parts corresponding to pre-buckle and post-buckle behaviour of the struts. Two design points are selected to show the range of responses.

model hyperparameters, including the kernel's length scales and variance, was performed using Scipy optimizer, which minimized the model's negative log marginal likelihood. The optimization process was terminated based on the maximum number of iterations and an internal tolerance criterion. The model was trained using 1100 data points, with the remaining 400 samples reserved for testing.

3. Results

3.1. Quasi static experimental testing

In the stress-strain curve presented in Fig. 3a, the mechanical response of Group 6 under gradual increase of compressive apparent strain to 80 % is divided into distinct regions. Initially, within the linear region (0–5 % strain), the stress increases proportionally with strain, indicative of elastic behavior. As the strain progresses into the plateau region (10–40 %), the stress reaches a critical point at which the struts

start to buckle causing a snap through, which causes the stress to remain relatively constant or decrease, signifying the post buckle non-linear behavior of the metamaterial. Beyond 40 % strain, the material transitions into the early densification region, where the struts make contact, causing a gradual increase in stress. This trend becomes more prominent in the densification region (70–80 %), where stress increases drastically due to compaction of the struts to the top and bottom discs and to each other.

The results of the porosity (P) and surface area-to-volume ratio (S/V) measurements are shown in Fig. 4. A reduction in P was observed from Group 1 to 3, decreasing from 95.4 % to 81 %, and from 98.6 % to 91.45 % for $d_{cell} = 20$ mm and $d_{cell} = 40$ mm, respectively; from Group 4 to 6, decreasing from 96.6 % to 87 %, and from 98.6 % to 94.3 % for $d_{cell} = 20$ mm and $d_{cell} = 40$ mm, respectively; and from Group 7 to 9, decreasing from 97.2 % to 90.4 %, and from 98.7 % to 95.6 %, for $d_{cell} = 20$ mm and $d_{cell} = 40$ mm, respectively. An increasing trend in P was noted across Groups 1, 4, and 7 (95.4 % to 97.2 % for $d_{cell} = 20$ mm, and

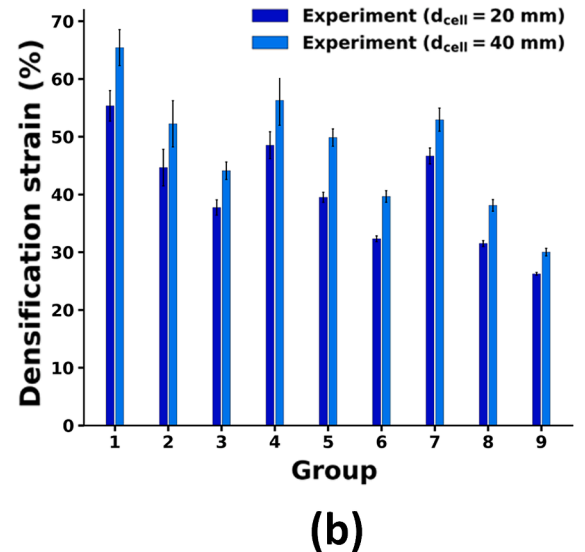
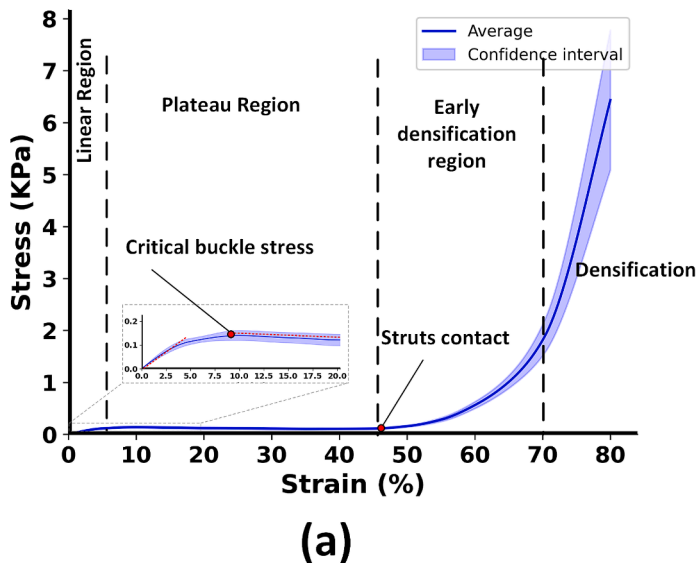


Fig. 3. (a) Stress-strain curve of the OISCS under 80 % compression strain with average and confidence intervals corresponding to 6 tested samples of the Group 6. (b) Densification strain for each group measured from experiment.

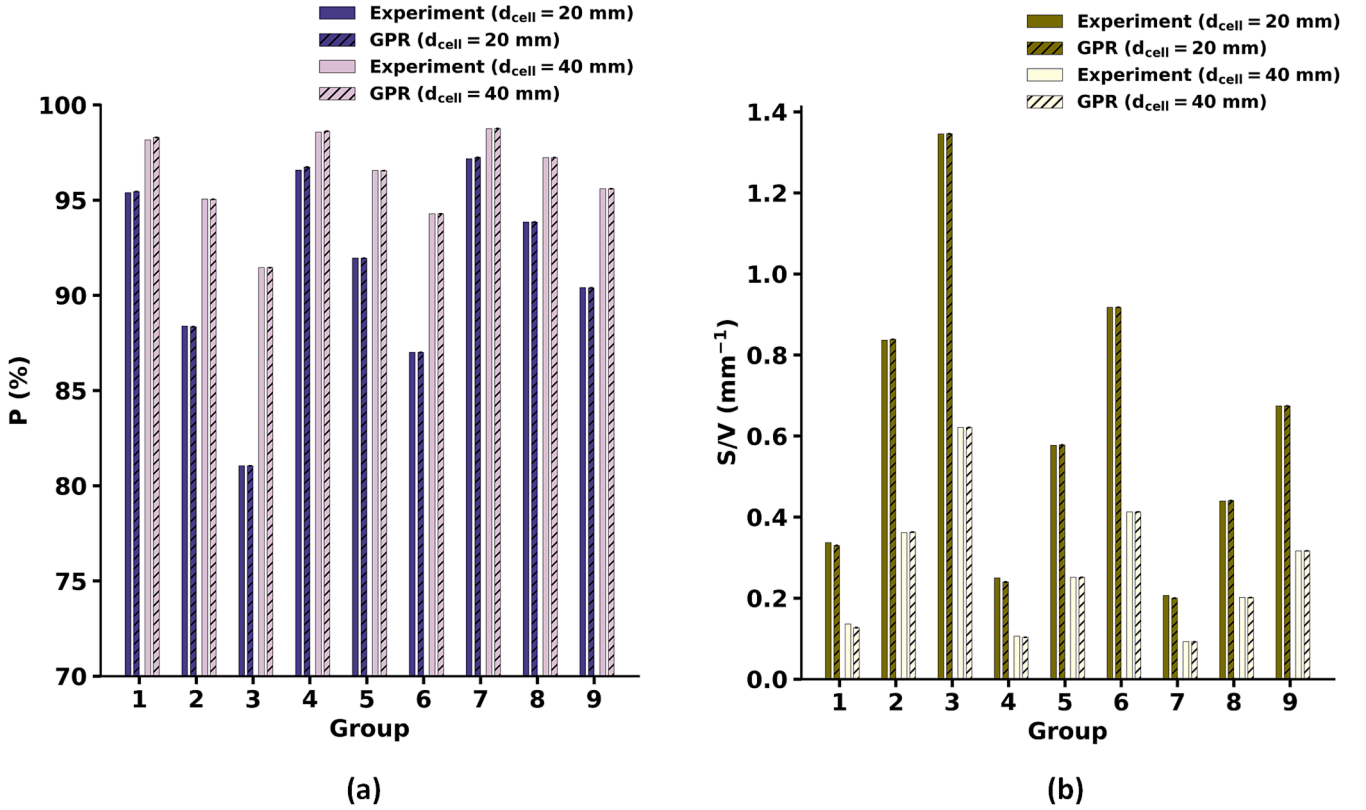


Fig. 4. Comparison of P and S/V across the nine selected Groups. Each group has two designs that only differ in d_{cell} . Predicted values from the trained GPR models are presented beside each calculated value for comparison. (a) The porosity values, with Group 7 exhibiting the highest porosity and Group 3 showing the lowest. (b) The surface area to volume ratio values, where Group 3 demonstrates the highest value and Group 7 the lowest. These metrics highlight the structural differences between Groups.

98.2 % to 98.7 % for $d_{cell} = 40$ mm), Groups 2, 5, and 8 (88.4 % to 93.85 % for $d_{cell} = 20$ mm, and 95.1 % to 97.2 % for $d_{cell} = 40$ mm), and Groups 3, 6, and 9 (81 % to 90 % and for $d_{cell} = 20$ mm, and 91.4 % to 95.6 % for $d_{cell} = 40$ mm). Notably, Group 7 exhibited the highest porosity at 97.2 % ($d_{cell} = 20$ mm) and 98.7 % ($d_{cell} = 40$ mm), while Group 3 showed the lowest at 81 % ($d_{cell} = 20$ mm) and 91.4 % ($d_{cell} = 40$ mm). In contrast, S/V increased from Group 1 to 3 (0.34 mm^{-1} to 1.34 mm^{-1} for $d_{cell} = 20$ mm, and 0.14 mm^{-1} to 0.62 mm^{-1} for $d_{cell} = 40$ mm), Group 4 to 6 (0.25 mm^{-1} to 0.92 mm^{-1} for $d_{cell} = 20$ mm, and 0.11 mm^{-1} to 0.41 mm^{-1} for $d_{cell} = 40$ mm), and Group 7 to 9 (0.21 mm^{-1} to 0.67 mm^{-1} for $d_{cell} = 20$ mm, and 0.2 mm^{-1} to 0.67 mm^{-1} for $d_{cell} = 40$ mm). A decreasing trend in S/V was found for Groups 1, 4, and 7 (0.34 mm^{-1} to 0.21 mm^{-1} for $d_{cell} = 20$ mm, and 0.14 mm^{-1} to 0.09 mm^{-1} for $d_{cell} = 40$ mm), Groups 2, 5, and 8 (0.84 mm^{-1} to 0.44 mm^{-1} for $d_{cell} = 20$ mm, and 0.36 mm^{-1} to 0.2 mm^{-1} for $d_{cell} = 40$ mm), and Groups 3, 6, and 9 (1.34 mm^{-1} to 0.67 mm^{-1} for $d_{cell} = 20$ mm, and 0.62 mm^{-1} to 0.32 mm^{-1} for $d_{cell} = 40$ mm). Group 7 had the lowest S/V at 0.21 mm^{-1} ($d_{cell} = 20$ mm) and 0.09 mm^{-1} ($d_{cell} = 40$ mm), while Group 3 exhibited the highest S/V at 1.34 mm^{-1} ($d_{cell} = 20$ mm) and 0.62 mm^{-1} ($d_{cell} = 40$ mm).

The stress-strain responses of the nine groups, shown in Fig. 5 and quantified in Fig. 6, demonstrate that as the number of struts increased from 8 to 20 ($\phi = 5^\circ$), E increased from 5.3 ± 1.7 Pa to 41.8 ± 9.1 Pa, and from 2.5 ± 1.1 to 23.4 ± 6.1 for $d_{cell} = 20$ mm and $d_{cell} = 40$ mm, respectively, the buckling stress increased from 46.6 ± 6.5 Pa to 274.3 ± 53.7 Pa, and from 22.3 ± 8.3 to 155.6 ± 55.1 , for $d_{cell} = 20$ mm and $d_{cell} = 40$ mm, respectively, U increased from $0.7 \pm 0.3 \text{ kJ/m}^3$ to $5.9 \pm 1 \text{ kJ/m}^3$, and from $0.5 \pm 0.1 \text{ kJ/m}^3$ to $2.9 \pm 0.5 \text{ kJ/m}^3$, for $d_{cell} = 20$ mm and $d_{cell} = 40$ mm, respectively, and the densification limit decreased from 55.3 ± 2.6 % to 37.7 ± 1.3 %, and from 65.4 ± 3.1 to 44.1 ± 1.5 , for $d_{cell} = 20$ mm and $d_{cell} = 40$ mm, respectively. This trend was

consistent for other constant ϕ values of 25° and 45° . As ϕ increased from 5° to 45° with a constant $n = 8$, E decreased from 5.3 ± 1.7 Pa to 1.8 ± 1.1 Pa, and from 2.5 ± 1 to 0.8 ± 0.5 , for $d_{cell} = 20$ mm and $d_{cell} = 40$ mm, respectively, the buckling stress decreased from 46.6 ± 6.5 Pa to 25.5 ± 5.3 Pa, and from 22.3 ± 8.3 to 9.6 ± 6 , for $d_{cell} = 20$ mm and $d_{cell} = 40$ mm, respectively, U increased from $0.7 \pm 0.3 \text{ kJ/m}^3$ to $0.3 \pm 0.1 \text{ kJ/m}^3$, and from $0.5 \pm 0.1 \text{ kJ/m}^3$ to $0.3 \pm 0.1 \text{ kJ/m}^3$, for $d_{cell} = 20$ mm and $d_{cell} = 40$ mm, respectively, and the densification limit decreased from 55.3 ± 2.6 % to 46.6 ± 1.4 %, and from 65.4 ± 3.1 to 52.9 ± 2 , for $d_{cell} = 20$ mm and $d_{cell} = 40$ mm, respectively. This trend was also observed for $n = 14$ and $n = 20$. Group 7 exhibited the lowest E (1.8 ± 1.1 Pa for $d_{cell} = 20$ mm, and 0.8 ± 0.4 Pa for $d_{cell} = 40$ mm) and U ($0.5 \pm 0.1 \text{ kJ/m}^3$ for $d_{cell} = 20$ mm, and $0.3 \pm 0.1 \text{ kJ/m}^3$ for $d_{cell} = 40$ mm), while Group 3 showed the highest E (41.8 ± 8.9 Pa for $d_{cell} = 20$ mm, and 23.4 ± 6.1 for $d_{cell} = 40$ mm) and U ($5.9 \pm 1 \text{ kJ/m}^3$ for $d_{cell} = 20$ mm, and $2.9 \pm 0.5 \text{ kJ/m}^3$ for $d_{cell} = 40$ mm). Similarly, Group 7 had the lowest buckling stress (25.5 ± 5.3 Pa for $d_{cell} = 20$ mm, and 9.7 ± 5 Pa for $d_{cell} = 40$ mm), and Group 3 had the highest (274.3 ± 53.7 Pa for $d_{cell} = 20$ mm, and 155.6 ± 55.1 Pa for $d_{cell} = 40$ mm) (Fig. 3b). Group 9 had the lowest densification limit (26.2 ± 0.2 % for $d_{cell} = 20$ mm, and 30 ± 0.7 % for $d_{cell} = 40$ mm), and Group 1 had the highest at 55.3 ± 2.6 % for $d_{cell} = 20$ mm, and 65.4 ± 3.1 % for $d_{cell} = 40$ mm (Fig. 3b).

3.2. Validation of the FE model

The comparison of the simulation with the experiments for the early response of the metamaterial (<25 % strain) showed that the simulation captured the experimental trend (Fig. 5). Strain energy density in the simulation corresponded to the experiments. However, deviation between the simulation and experiment was found in elastic modulus in

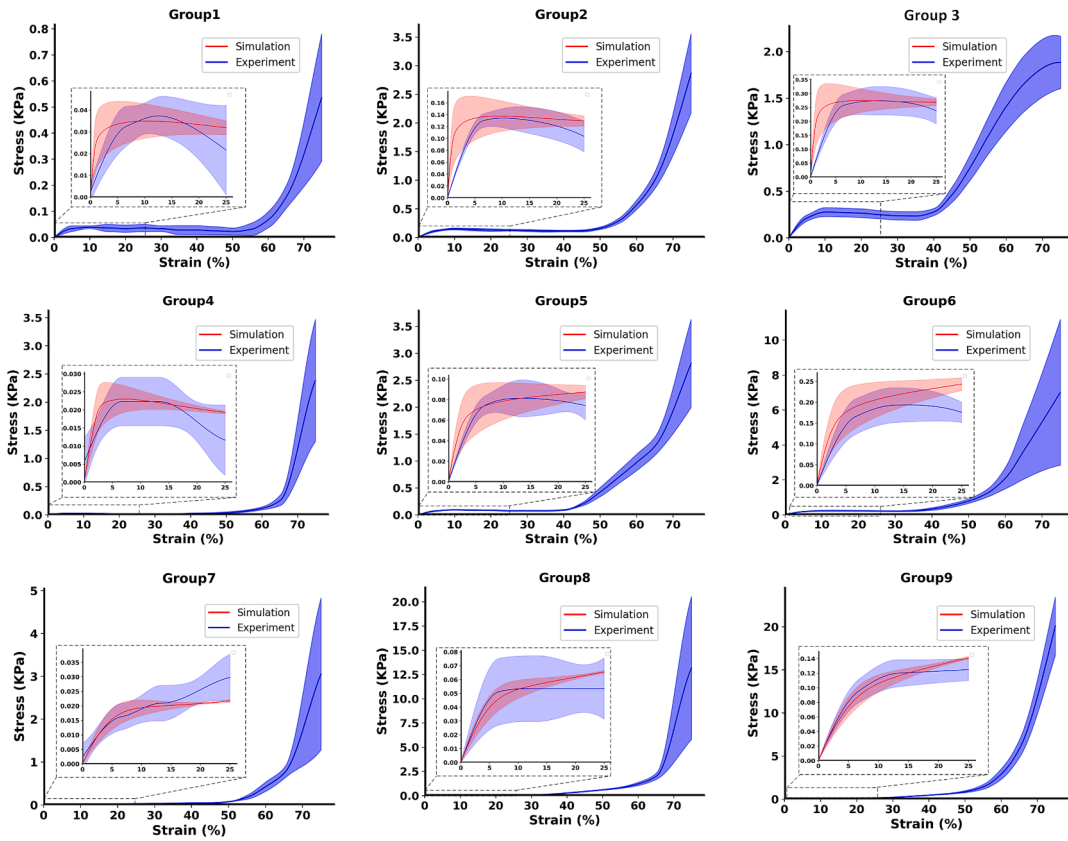


Fig. 5. Stress-strain response of each design group with $d_{cell} = 20$ mm to Quasi-static compressive strain. For each group, the experimental data (red) and simulation results (blue) are plotted along with their respective confidence intervals, represented by shaded areas. Each subplot includes the main stress-strain curve and an inset focusing on the early mechanical response. The comparison of the simulation and the experiment are limited to 25 % strain, which is before any contact.

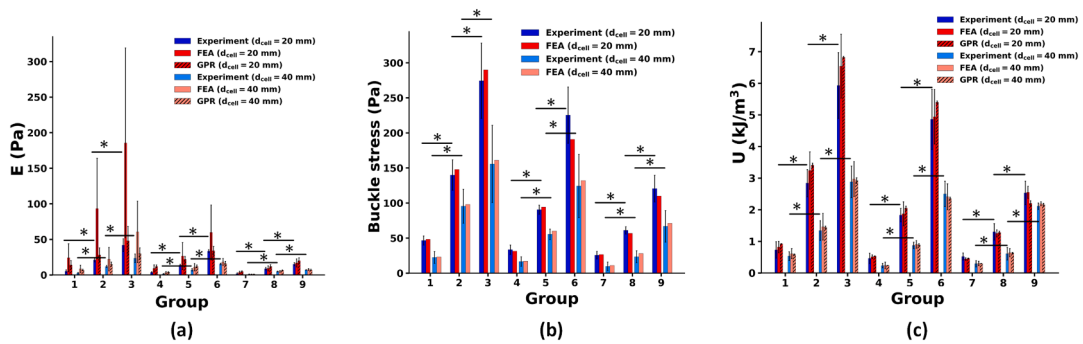


Fig. 6. (a) Elastic modulus measured from each group compared to the corresponding simulation, and predicted GPR model outcomes. (b) Buckle stress measured from each group compared to the corresponding simulation outcome. (c) Densification strain for each group measured from experiment (* $P < 0.05$). (c) U measured from each group compared to the corresponding simulation, and predicted GPR model outcomes.

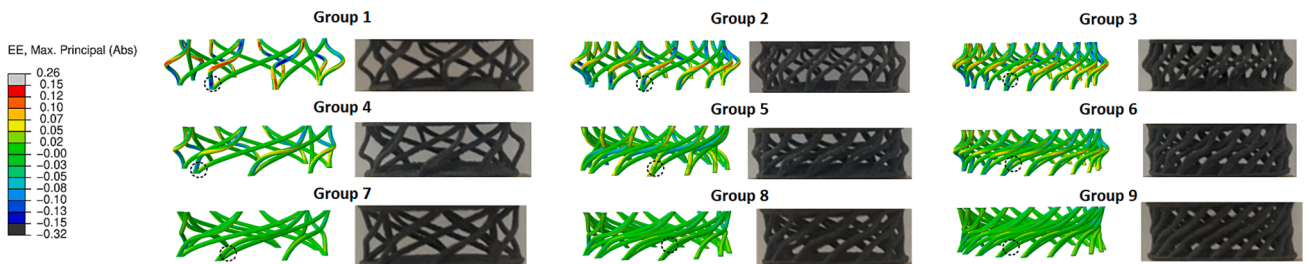


Fig. 7. Distribution of maximum principal strain in the struts for each selected design group. Strains more than 15 % are in gray and black for tension and compression, respectively. Dotted circle shows the location of the critical region in each group. The deformation of struts in each simulation is compared with its corresponding experiment.

Group 1, Group 2, and Group 3 all with a similar ϕ of 5° .

3.3. Strain distribution

Fig. 7 shows the FE analysis of the nine selected designs. Both tensile and compressive strain were found in the struts suggesting a combination of bending, tension and compression force acting on the strut network. It was found that under the same amount of displacement (structural strain), the struts in Group 1 with the fewest n and smallest ϕ among other groups, experienced greatest compressive and tensile strains with values around 15 % along the short strut. Increasing the number of struts resulted in a marginal reduction of strain. The smallest strains with values less than 2 % were found in Group 9. Moreover, a critical strain region was found at the connection point of the struts, where peak strains more than 15 % for Group 1 occurred. In contrast with the trend of strain in the struts, maximum strains in the critical region increased as the number of struts increased. Increasing ϕ reduced the maximum strains at the critical region.

3.4. Cyclic response

Stress–strain response of Group 6 under 200 cycles of compressive strain (10 %, 30 %, 50 %, and 70 %) is shown in Fig. 8a as an example to show the recovery capability of the metamaterial. The plots showed that after the first 10 cycles the loading and unloading paths overlap. As the strain exceeded the densification limit of Group 6 (after 32 % strain), for 50 % and 70 % strains cycles, the hysteresis area became larger, which was mainly attributed to the part of the stress–strain graphs that corresponded to the densification region. It also took more than 20 to 50 cycles to reach the overlapping of the loading and unloading paths. Fig. 9b shows the reduction in the maximum stress as the number of cycles increases. Same behavior was observed for other Groups.

3.5. GPR and sensitivity analysis

The output dataset for P , S/V , E , U , and ϵ_{\max} , obtained from the virtual lab, is illustrated in Fig. 9. P and S/V exhibit considerable variation, ranging from 49.7 % to 99.9 % and 0.04 mm^{-1} to 2.8 mm^{-1} , respectively. E spanned from 0.1 Pa to 1.8 kPa, while ϵ_{\max} ranged from 1.2 % to 42.5 %. U ranged from 0.005 kJ/m^3 to 23.1 kJ/m^3 . A noticeable trend was observed, where higher P generally correlated with lower S/V ratios. Additionally, a weak relationship was found between lower P and

higher E and U values. Samples with higher E and U also exhibited increased ϵ_{\max} . A slight trend of increasing ϵ_{\max} was observed in samples with lower P .

Fig. 10 summarizes the variance-based Sobol global sensitivity analysis. The sensitivity analysis of the input variables d_{strut}/h , ϕ , n , and d_{cell}/h revealed that ϕ had the strongest influence on E , with d_{cell}/h , d_{strut}/h and n playing a lesser role. ϵ_{\max} was highly affected by d_{cell}/h and d_{strut}/h , while ϕ and n had minimal impact. U was highly influenced by ϕ and d_{strut}/h , while d_{cell}/h had less impact, and n had the lowest impact. For P , d_{strut}/h and d_{cell}/h had a greater influence than n , and both n and ϕ had a moderate effect. S/V was primarily influenced by d_{cell}/h , n and ϕ , with d_{strut}/h showing a weaker influence.

GPR models for each output parameter were created. Testing the trained models showed high quality of regression for all the models ($R^2=0.98$). GPR analysis outcomes showed that predicted P , S/V , E , U , and ϵ_{\max} corroborated with the sensitivity analysis results and the experimental data (Fig. 4a and b, and Fig. 6a and c). Lowest porosity was predicted to be achievable at $d_{\text{strut}}/h = 0.7$, $\phi = 0$, and $n = 36$. As the d_{strut}/h approached towards 0.01, and n to 6, or ϕ to 60° , P reached values above 90 % (Fig. 11a). Increasing d_{cell}/h shifted the P to higher values with minimum values in $d_{\text{cell}}/h = 1$ and maximum values in $d_{\text{cell}}/h = 4$.

S/V was maximized as n approached 36 and ϕ closer to 0. d_{strut}/h had marginal effect on S/V , where increasing d_{strut}/h to 0.07 will cause higher S/V (Fig. 11b). Increasing d_{cell}/h shifted S/V to lower values with maximum values in $d_{\text{cell}}/h = 1$ and minimum values in $d_{\text{cell}}/h = 4$. A wide range of elasticity, from 0.1 Pa to 7 kPa, was predicted to be achievable by simply changing the four input design variables (Fig. 12a). Highest E of 23 Kpa was predicted to be achieved at $d_{\text{strut}}/h = 0.07$, $\phi = 0$, $n = 35$, and $d_{\text{strut}}/h = 1$. Increasing d_{strut}/h and n increased E while increasing ϕ reduced E . The effect of d_{strut}/h and ϕ on E was more prominent compare to the effect of n . Increasing d_{cell}/h shifted E to lower values with maximum values in $d_{\text{cell}}/h = 1$ and minimum values in $d_{\text{cell}}/h = 4$. Strain energy absorbed was predicted to range from near zero values to 34 kJ/m^3 . Similar to E , highest U was predicted to be achieved at $d_{\text{strut}}/h = 0.07$, $\phi = 0$, $n = 35$, and $d_{\text{strut}}/h = 1$ (Fig. 12b). Increasing d_{strut}/h , and reducing ϕ increased U while increasing n had minor effect on the increase of U . Increasing d_{cell}/h reduced U similar to E . Maximum local strain in the OISCM was highly sensitive to the change in d_{cell}/h and d_{strut}/h , while showing low dependency to ϕ and n (Fig. 12c). ϵ_{\max} ranged from 2 % to 36 % with the maximum achieved at the highest $d_{\text{strut}}/h = 0.07$, lowest $\phi = 0$, highest $n=36$, and lowest d_{cell}/h .

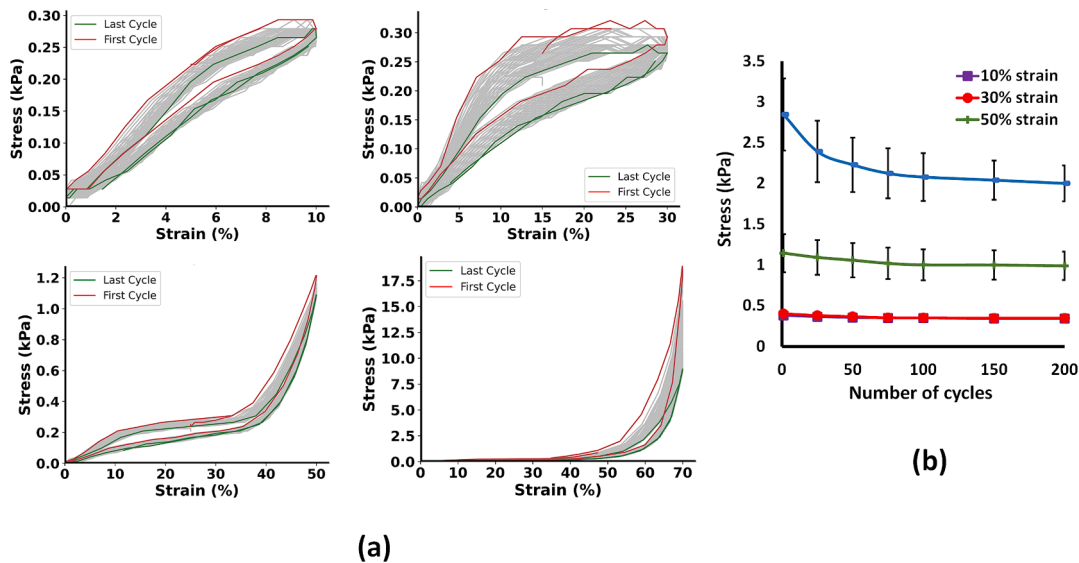


Fig. 8. (a) Stress–strain response of Group 6 to cyclic loading with sequential strain change of 10 % (top left), 30 % (top right), 50 % (bottom left), and 70 % (bottom right). (b) Change in the maximum stress at each specific loading cycle.

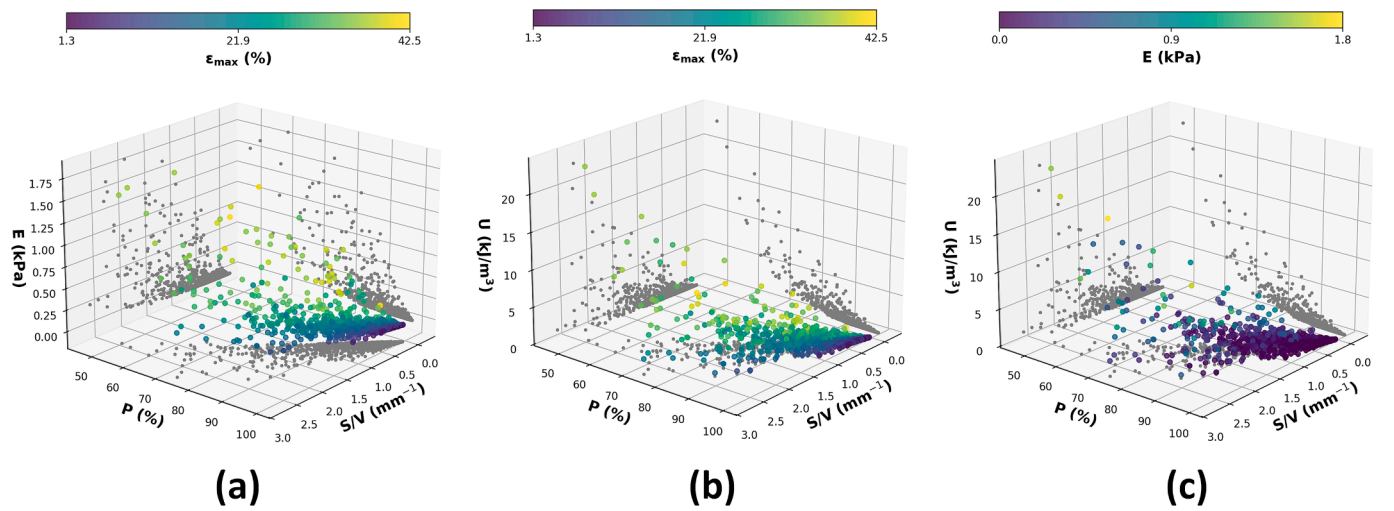


Fig. 9. Distribution and correlation between outputs for the set of 1500 samples in the design space. (a) Distribution of P , S/V , E , and ϵ_{\max} . The color gradient represents the values of ϵ_{\max} (%). (b) Distribution of P , S/V , U , and ϵ_{\max} . The color gradient represents the values of ϵ_{\max} (%). (c) Distribution of P , S/V , U , and E . The color gradient represents the values of E (kPa). Gray points indicate the projection of each data point onto the P - S/V , S/V - E , E - P , S/V - U , P - U planes, highlighting trends within these two-dimensional slices.

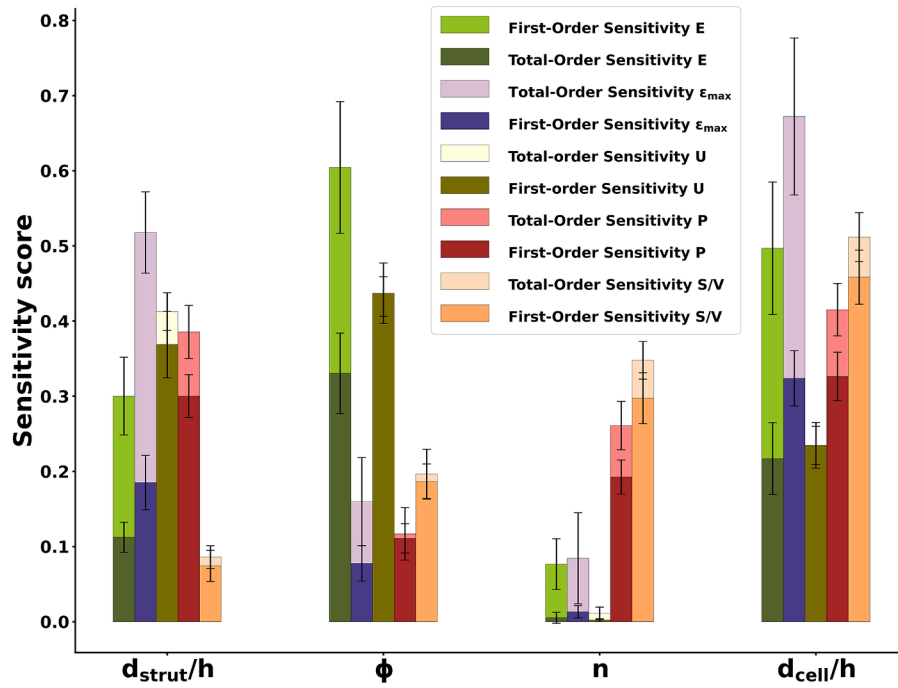


Fig. 10. Sensitivity scores for the four input variables, d_{strut}/h , ϕ , n , and d_{cell}/h showing the influence of each variable on the output of interest. Sensitivity score values near to 1 shows strong influence of that variable to the output of interest.

$h = 1$ in the design space.

4. Discussion

In this study we aimed at introducing a new metamaterial design inspired from an origami pattern. The goal was to assess the super compressibility of the metamaterial and check the range of programmability of the design for potential use in tissue engineering.

The tested OISC exhibited stress-strain response under quasi static compression similar to porous architectures that have been studied before [11,13,34] (Fig. 3a). Control buckling has been previously implemented in the design of metamaterial [21,34]. It has been reported that micro-architected metamaterials for tissue engineering can undergo

buckling modes due to biological forces from cells or external force [3,34]. These buckling modes can improve the metamaterial's compliance and permeability [3,34], which is advantageous for cell ingrowth in a dynamic physiological environment. The distinguishing feature of the OISC design is the negative stiffness observed after the linear region of the stress-strain graphs and post buckling and full recoverable flat-foldability. This behavior inherent from the bi-stable properties of Kresling origami [16,17,35] was more prominent when ϕ was closer to zero (Fig. 5 Groups 1 and 4). However due to the monolithic printing of the metamaterial and having fixed joints at the attachment point of struts to discs (Fig. 1d), some strain was stored in the joint. This caused the second stable point to be a bit above zero stress. Therefore, bi-stability of the OISC depends on the type of the fabricated struts

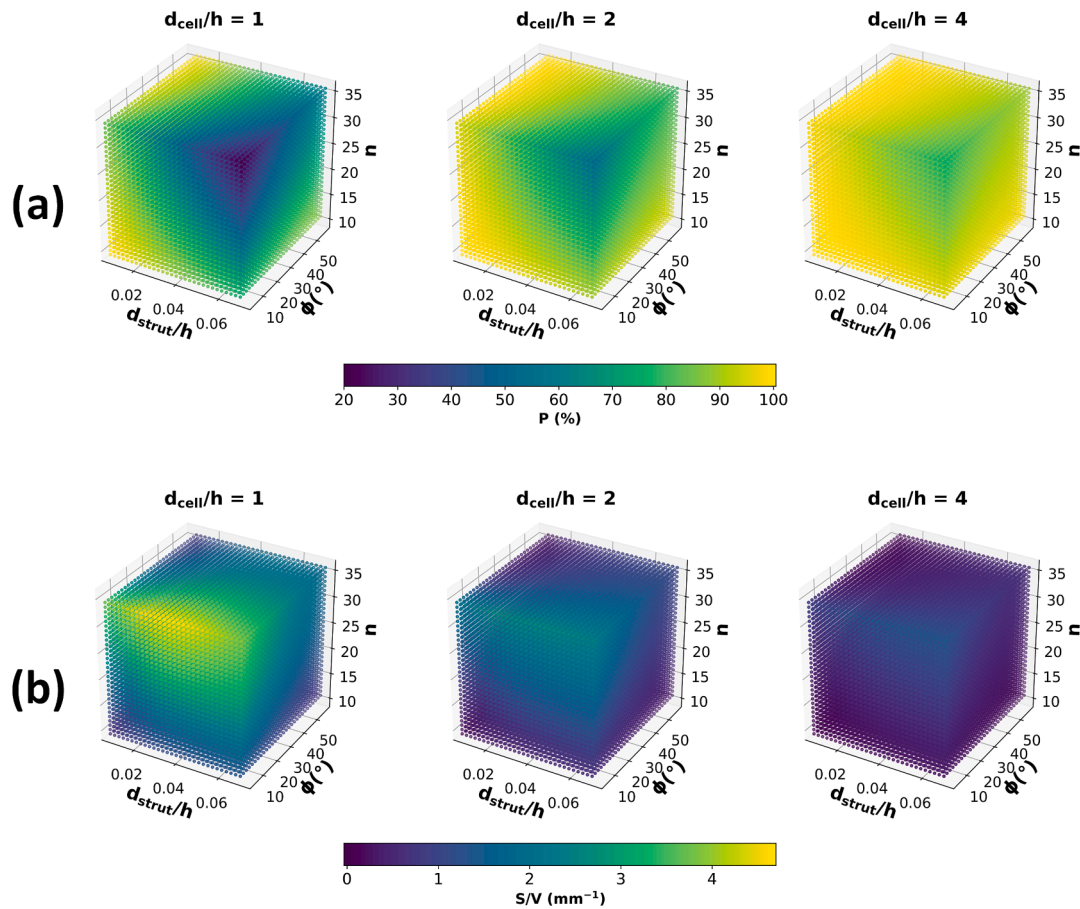


Fig. 11. GPR prediction illustrating the effect of varying input parameters d_{strut}/h , ϕ , n , and d_{cell}/h on two key structural variables: (a) P , and (b) S/V . The color gradient in each plot represents the respective output value across the design space.

joints. The flat foldability of Kresling origami is partly owed to using thin papers with thickness around 0.05–0.1 mm [17]. Therefore, we expect that as the strut diameter d_{strut} (Fig. 1a) becomes closer to the thickness of a regular paper, flat foldability can be achieved even without changing the strut joint type. This is because less stress will be required to deform the thinner struts at the joints. High compressibility of OISC is advantageous for designing scaffolds for special procedures such as distraction osteogenesis, which is the gradual elongation of a very small osteotomy to reach a large gap in bone while bone starts to form in the gap [36]. OISC can be inserted in the gap in the compressed configuration and then be gradually deployed with the elongation of the gap and help the healing.

To ensure the functionality of the metamaterial, it is necessary to make sure that the OISC can withstand loads during the deformation of the struts without failure. In Fig. 12c, the dependency of maximum strain to the input variables was demonstrated for the material used in this study. Furthermore, results of the cyclic loading tests showed a good strain recovery at different strain levels and full recovery after a few cycles (Fig. 8b). There was a trend of reduction in the maximum stress as the number of cycles increased until peak stresses overlap each other. This trend suggests initial microstructural adjustments within the OISC, leading to stabilization after multiple cycles. These adjustments required more cycles when strut contacts are included with 50 % and 70 % strain, which indicates the importance of preconditioning. Flexa grey is a material that has strain failure limit of 120 %, which is above the maximum values of strains that was predicted in the design space. This explains why no failure happened in the experiments. Similarly, biocompatible materials such as high molecular weight PCL are known for their large strain tolerance and have high elastic modulus 70 MPa

[11,26]. These biocompatible materials can be used to manufacture OISC that has biological applications. Same predictive model as Fig. 12c can be created for other materials using the data-driven Bayesian machine learning that was implemented in this study to help choosing designs with lower risk of failure.

It was demonstrated that, within the design space of OISC, porosity and S/V , can alter by 50 % (about 101 % increase compared to the minimum amount) and 2.76 mm^{-1} (about 70 times more than the minimum amount), respectively (Fig. 9 and Fig. 11). In the context of bone tissue engineering, the porosity of scaffolds is a crucial factor in their design, significantly influencing both biological and mechanical properties. High porosity has been reported to facilitate cell migration, proliferation, and differentiation, as well as the diffusion of nutrients and oxygen, essential for cell viability and vascularization [12,37]. A porosity of around 80 % has been reported to have the best bone formation [38]. Additionally, a higher S/V provides more surface area for cell attachment and growth factor retention [37], which can further promote osteogenic activity. However, some studies reported that a lower S/V favors bone growth in large bone defects [9]. Wide range of structural properties in OISC design can be used to further investigate the impact of P and S/V on the biology of bone healing.

Although, altering the P and S/V can be beneficial for biological functions, they can compromise the mechanical properties [39]. By comparing predictive models in Figs. 11 and 12 it was shown that with the OISC design it is possible to achieve a specific elastic modulus and energy absorption with a range of densities and S/V , and vice versa. It is important to ensure that the scaffold can support the intended physiological loads while promoting tissue regeneration. The challenge in scaffold design lies in achieving sufficient porosity and S/V to enhance

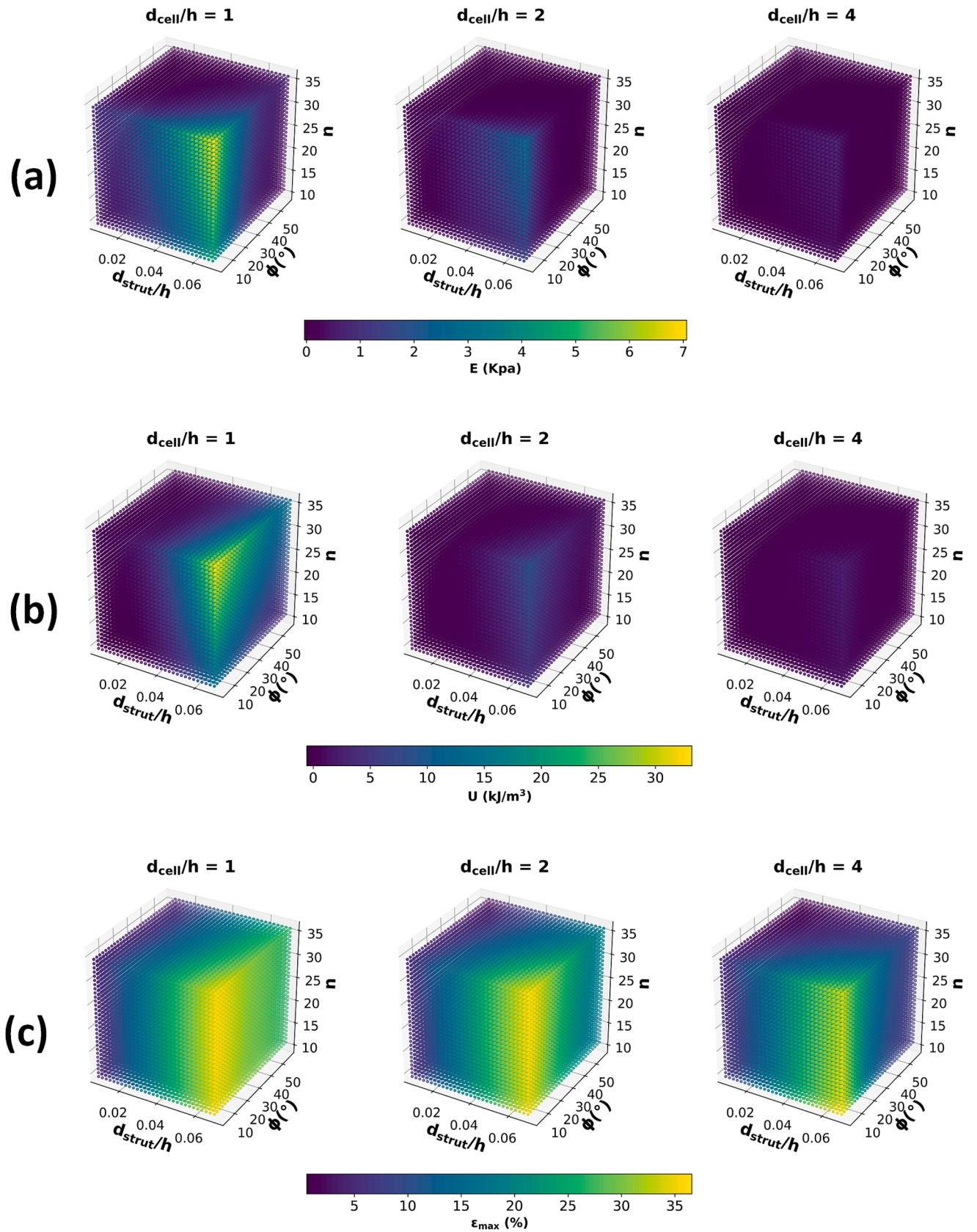


Fig. 12. GPR prediction illustrating the effect of varying input parameters d_{strut}/h , ϕ , n , and d_{cell}/h on key mechanical variables: (a) E , (b) U , and (c) ϵ_{max} . The color gradient in each plot represents the respective output value across the design space.

biological performance while maintaining the necessary mechanical properties to fulfill the scaffold's mechanical demands. Our predictive model of OISCM elasticity and strain energy (Fig. 12a and b) can be used for optimization based on biological evidence in the future.

The elastic modulus in the linear region captures the performance of the metamaterial under small deformations, particularly when the structure is fully deployed. While E may not reflect the total deformation capacity of the structure, it remains significant for applications where micromotion plays a critical role after deployment of OISCS. For instance, in clinical applications such as distraction osteogenesis (DO) or bone elongation, micromotion at the osteotomy site after complete elongation is a crucial factor influencing bone healing [40,41]. In such cases, E represents the mechanical performance of the metamaterial and its potential for enhancing bone regeneration. Additionally, strain energy complements the elastic modulus by capturing the overall mechanical response, ensuring structural integrity while enhancing mechanical stimuli to the neighboring tissues and cells. Together, these properties provide a comprehensive understanding of the metamaterial's potential to support and promote bone regeneration.

A wide spectrum of elastic modulus, from 1 Pa to 20 GPa can be found inside the human body [42]. Therefore, tunability of stiffness in the design of scaffolds is important in order to have a design that can adapt to different applications. We showed that our OISCM can have up to 18,000 fold change in elastic modulus, from 0.1 Pa to 1.8 kPa, by tuning the four key design parameters, while preserving super-compressibility. We hypothesize that by choosing a stiffer material, it is possible to offset this range of elasticity to MPa and GPa, which can be investigated in future studies. Adding other input variables such as bulk elastic modulus, that were considered constant in this study, can help to gain a more coherent characterization of the design. The currently developed predictive FEA combined with GPR enables us to explore within the entire design space of scaffolds providing a robust framework for optimizing the design for specific tissue engineering application.

5. Limitations

The FE model developed in this study was limited to strains less than 25 % to avoid contact simulation, which significantly reduced the computational cost. This simplification was necessary to preserve the efficiency of the virtual lab and avoid convergence issues. Although the simulation captured the early non-linear behavior of OISCM there were some inconsistencies between the FE analysis and experiment. Uncertainties in the geometry and mechanical properties of additively manufactured samples can highly influence strain-stress response of the metamaterial. For instance, d_{strut} which highly influenced E , was considered to have constant value in the printed samples while it could have deviated from the CAD models due to the length of the struts compare to their cross section. Despite, printing angle could have changed the bulk elastic modulus, a constant Young's modulus was assigned to all the samples. Finally, the high sensitivity of the FE models to the initial magnitude of geometrical imperfection, which can give a wide range of values for elastic modulus as depicted in Fig. 5 Group 2 and 3.

6. Conclusion

This study introduced a new metamaterial design inspired from origami, demonstrating its significant tunability in porosity and surface-to-volume ratio (S/V), which are crucial for tissue engineering. The OISCM's adjustable mechanical properties and bi-stable behavior make it suitable for applications like distraction osteogenesis, where no regular scaffold can be used. FE data-driven Bayesian machine learning model predicted a wide range of elastic moduli and strain energy density, that can be achieved with this design. This versatility in the mechanical properties of OISCM makes it suitable for a wide range of tissue engineering applications. Future research should explore the effect of

including additional variables to widen the programmability and further optimize the design for specific applications.

CRedit authorship contribution statement

M.A. Bagheri: Writing – original draft, Visualization, Validation, Software, Resources, Project administration, Methodology, Investigation, Formal analysis, Data curation, Conceptualization. **C.E. Aubin:** Writing – review & editing, Supervision, Methodology, Funding acquisition, Formal analysis, Conceptualization. **M.L. Nault:** Writing – review & editing, Supervision. **I. Villemure:** Writing – review & editing, Supervision, Resources, Funding acquisition.

Declaration of competing interest

The authors declare the following financial interests/personal relationships which may be considered as potential competing interests: Mohammad Ali Bagheri has patent DEFORMABLE SCAFFOLD WITH MECHANICAL TUNABILITY FOR BONE TISSUE ENGINEERING pending to Polytechnique Montreal. If there are other authors, they declare that they have no known competing financial interests or personal relationships that could have appeared to influence the work reported in this paper.

Acknowledgements

This study was supported by a project grant from the TransMedTech Institute (Canada First Research Excellence Fund) and by a scholarship from the CREATE program of the Natural Sciences and Engineering Research Council of Canada (NSERC).

Appendix A. Supplementary data

Supplementary data to this article can be found online at <https://doi.org/10.1016/j.matdes.2025.113701>.

Data availability

The data that has been used is confidential.

References

- [1] E. Dogan, et al., 3D printing metamaterials towards tissue engineering, *Appl. Mater. Today* 20 (2020) 100752.
- [2] A.V. Do, et al., 3D printing of scaffolds for tissue regeneration applications, *Adv. Healthc. Mater.* 4 (12) (2015) 1742–1762.
- [3] C. Wang, et al., Micro-engineered architected metamaterials for cell and tissue engineering, *Materials Today Advances* 13 (2022) 100206.
- [4] C. Garot, G. Bettega, C. Picart, Additive manufacturing of material scaffolds for bone regeneration: toward application in the clinics, *Adv. Funct. Mater.* 31 (5) (2021).
- [5] A.-M. Pobloth, et al., Mechanobiologically optimized 3D titanium-mesh scaffolds enhance bone regeneration in critical segmental defects in sheep, *Sci. Transl. Med.* 10 (423) (2018).
- [6] J.J. Li, et al., A novel bone substitute with high bioactivity, strength, and porosity for repairing large and load-bearing bone defects, *Adv. Healthc. Mater.* 8 (8) (2019) 1801298.
- [7] M. Laubach, et al., The concept of scaffold-guided bone regeneration for the treatment of long bone defects: current clinical application and future perspective, *J. Funct. Biomater.* 14 (7) (2023).
- [8] S. Wang, et al., Honeycomb structure is promising for the repair of human bone defects, *Mater. Des.* 207 (2021).
- [9] M. Jaber, et al., PCL strut-like scaffolds appear superior to gyroid in terms of bone regeneration within a long bone large defect: an in silico study, *Front. Bioeng. Biotechnol.* 10 (2022) 995266.
- [10] E. Daskalakis, et al., Bone bricks: the effect of architecture and material composition on the mechanical and biological performance of bone scaffolds, *ACS Omega* 7 (9) (2022) 7515–7530.
- [11] Z. Meng, et al., Design and additive manufacturing of flexible polycaprolactone scaffolds with highly-tunable mechanical properties for soft tissue engineering, *Mater. Des.* 189 (2020).
- [12] L. Wang, et al., Single-parameter mechanical design of a 3D-printed octet truss topological scaffold to match natural cancellous bones, *Mater. Des.* 209 (2021).

- [13] N. Yang, et al., New network architectures with tunable mechanical properties inspired by origami, *Mater. Today Adv.* 4 (2019).
- [14] A.L. Wickeler, H.E. Naguib, Novel origami-inspired metamaterials: design, mechanical testing and finite element modelling, *Mater. Des.* 186 (2020).
- [15] K. Yamaguchi, et al., Post-fabrication tuning of origami-inspired mechanical metamaterials based on Tachi-Miura Polyhedron, *Mater. Des.* 233 (2023).
- [16] A.S. Dalaq, M.F.J.M. Daqaq, and Design, Experimentally-validated computational modeling and characterization of the quasi-static behavior of functional 3D-printed origami-inspired springs, *Mater. Des.* 216 (2022) 110541.
- [17] Z. Zhai, Y. Wang, H.J.P.o.t.N.A.o.S. Jiang, Origami-inspired, on-demand deployable and collapsible mechanical metamaterials with tunable stiffness, *PNAS* 115 (9) (2018) 2032–2037.
- [18] X. Wang, et al., Multi-triangles cylindrical origami and inspired metamaterials with tunable stiffness and stretchable robotic arm, *PNAS Nexus* 2 (4) (2023).
- [19] H. Yasuda, et al., Origami-based tunable truss structures for non-volatile mechanical memory operation, *Nat. Commun.* 8 (1) (2017) 962.
- [20] D. Kong, et al., A biomimetic structural material with adjustable mechanical property for bone tissue engineering, *Adv. Funct. Mater.* (2023).
- [21] Z. Vangelatos, et al., Strength through defects: a novel Bayesian approach for the optimization of architected materials, *Science Advances* 7 (41) (2021) eabk2218.
- [22] C. Perier-Metz, et al., An in silico model predicts the impact of scaffold design in large bone defect regeneration, *Acta Biomaterialia* (2022).
- [23] M.O. Wang, et al., Evaluating 3D-printed biomaterials as scaffolds for vascularized bone tissue engineering, *Advanced Materials*. 27 (1) (2015) 138–144.
- [24] Y. Zheng, et al., Promotion of osseointegration between implant and bone interface by titanium alloy porous scaffolds prepared by 3D printing, *ACS Biomaterials Science and Engineering* 6 (9) (2020) 5181–5190.
- [25] C.M. Murphy, M.G. Haugh, F.J. O'Brien, The effect of mean pore size on cell attachment, proliferation and migration in collagen-glycosaminoglycan scaffolds for bone tissue engineering, *Biomaterials* 31 (3) (2010) 461–466.
- [26] J.H. Park, et al., 3D printing of poly-ε-caprolactone (PCL) auxetic implants with advanced performance for large volume soft tissue engineering, *Adv. Funct. Mater.* (2023).
- [27] S. Eshraghi, S.J.A.b. Das, Mechanical and microstructural properties of polycaprolactone scaffolds with 1-D, 2-D, and 3-D orthogonally oriented porous architectures produced by selective laser sintering, *Acta Biomaterialia* 6 (7) (2010) 2467.
- [28] C.W. Clenshaw, A.R.J.N.M. Curtis, A method for numerical integration on an automatic computer, *Numerische Mathematik* 2 (1960) 197–205.
- [29] M.A. Bessa, P. Glowacki, M.J.A.M. Houlder, Bayesian machine learning in metamaterial design: Fragile becomes supercompressible, *Advanced Materials* 31 (48) (2019) 1904845.
- [30] <ArcLength.pdf>.
- [31] J. Herman, W.J.J.o.O.S.S. Usher, SALib: an open-source Python library for sensitivity analysis. 2(9) (2017) 97.
- [32] A.G.d.G. Matthews, et al., GPflow: a Gaussian process library using TensorFlow. 18 (40) (2017) 1–6.
- [33] D.M.J. Dykstra, et al., Buckling metamaterials for extreme vibration damping, *Adv. Mater.* 35 (35) (2023) e2301747.
- [34] C. Wang, et al., Remodeling of architected mesenchymal microtissues generated on mechanical metamaterials, *3D Print. Addit. Manuf.* 9 (6) (2022) 483–489.
- [35] R. Tao, et al., 4D printed origami metamaterials with tunable compression twist behavior and stress-strain curves, *Compos. Part B: Eng.* (2020) 201.
- [36] M.A. Bagheri, et al., Finite element analysis of distraction osteogenesis with a new extramedullary internal distractor, *Comput. Methods Biomech. Biomed. Eng.* (2024) 1–15.
- [37] S.S. Lee, et al., Scaffolds for bone-tissue engineering, *Matter* 5 (9) (2022) 2722–2759.
- [38] P. Danilevicius, et al., The effect of porosity on cell ingrowth into accurately defined, laser-made, polylactide-based 3D scaffolds, *Appl. Surf. Sci.* 336 (2015) 2–10.
- [39] C.S. Ha, et al., Rapid inverse design of metamaterials based on prescribed mechanical behavior through machine learning, *Nat. Commun.* 14 (1) (2023) 5765.
- [40] J.M. García-Aznar, et al., Multiscale modeling of bone tissue Mechanobiology, *Bone* (2021) 116032.
- [41] D. Elliott, et al., A unified theory of bone healing and nonunion: BHN theory, *Bone Joint J.* 98 (7) (2016) 884–891.
- [42] C.F. Guimarães, et al., The stiffness of living tissues and its implications for tissue engineering, *Nat. Rev. Mater.* 5 (5) (2020) 351–370.